Finite Element Simulation of a Filament Stretching Extensional Rheometer

R. Sizaire V. Legat

20 January 1997

Abstract

The present paper is devoted to the numerical study of an extensional rheometer where a fluid sample is stretched between two plates. We use the FENE-CR model in order to simulate a Boger fluid stretched in the device. The analysis shows that the flow is not purely extensional, and that experimental data have to be analysed with caution, in particular if the extensional viscosity is not very high. In general, numerical simulations allow us to better understand experimental data.

1 Introduction

The measurement of extensional stresses is of critical importance to rheologists. For example, it is now well established that contraction flows are, in many cases, strongly influenced by extensional behaviour [1, 2]. The problem that arises then is to measure extensional data and to interpret such experimental data. The principle of the extensional rheometer is to try to expose the sample to a steady uniaxial extensional flow. Among other difficulties, the fact that the flow only approximates the uniaxial extensional flow, often prevents us to give a straightforward interpretation of the measurements. Of course, this problem also occurs for other types of rheometrical experiments. Therefore, an analysis of the flow can help to improve the interpretation of the experimental data. This type of analysis has already been made both by experimental observations and by numerical simulations [3, 4, 5, 6, 7, 8, 9].

In this paper, we present the results of a study of the filament stretching device used by Tirtaatmadja and Sridhar [10], Solomon and Muller [6] and McKinley and al. [7, 8, 9]. The device and the free-surface profile are schematically shown in Fig. 1. A constitutive equation is selected, and we use the material parameters identified by McKinley on the

basis of steady shear data. The model is then used to simulate the flow in the filament stretching rheometer and to compare numerical results with experimental observations. Finally, we can analyse the flow in detail and derive the conditions for which the device provides a flow close to uniaxial extension.

In section 2, we review the basic equations of a time-dependent free-surface viscoelastic problem. In particular, we briefly describe the FENE-CR constitutive equations. This constant shear-viscosity model appears to be a very efficient compromise between simplicity and physical modelling. In other words, we use the FENE-CR equations not as a *molecular* model but as a purely *macroscopic* one. In section 3, the numerical method applied for the simulation of the stretching device is briefly described. Finally, in section 4, we analyse the results for both Newtonian and viscoelastic flows. We derive what are the conditions to obtain an almost uniaxial extensional flow.

2 Basic Equations

2.1 The Viscoelastic Problem

Let us consider the flow of an incompressible fluid in a domain Ω. The partial differential equations governing the conservation of mass and momentum are

$$\left\{ \begin{array}{ll} \rho \dfrac{D\boldsymbol{v}}{Dt} - \nabla \cdot \sigma = \boldsymbol{f}, & \text{in } \Omega, \\ \\ \nabla \cdot \boldsymbol{v} = 0, & \text{in } \Omega, \end{array} \right. \tag{1}$$

where $\boldsymbol{v} = \boldsymbol{v}(\boldsymbol{x})$ is the velocity field, $\boldsymbol{x} = (x_1, x_2, x_3)^{\mathrm{T}}$ is the coordinate field, $\boldsymbol{f}$ denotes the body force per unit of volume, and σ is the Cauchy stress tensor. The fluid density is denoted by ρ and the operator D/Dt is the material derivative.

The Cauchy stress tensor σ is expressed as follows

$$\sigma = -p\mathbf{I} + \mathbf{T}_N + \mathbf{T}_V, \tag{2}$$

where p is the pressure, and $\mathbf{T}_N$ and $\mathbf{T}_V$ are the purely viscous and viscoelastic components of the stress tensor, respectively.

The viscous component $\mathbf{T}_N$ is given by

$$\mathbf{T}_N = 2\eta_N \underbrace{\frac{\nabla \boldsymbol{v} + \nabla^{\mathrm{T}} \boldsymbol{v}}{2}}_{\mathbf{D}}, \tag{3}$$

where η_N is the Newtonian viscosity and $\mathbf{D}$ is the strain rate tensor.

For the constitutive relationship of the viscoelastic component $\mathbf{T}_V$, we chose FENE-CR equations. In the FENE model introduced by Bird et al. [11], the polymer macromolecules are idealized as dumbbells suspended in a Newtonian solvent of viscosity η_N. In particular, the FENE model is characterized by the following non-linear spring law force for the dumbbell

$$f(R^2) = \frac{1}{1 - R^2/L^2}, \tag{4}$$

where L is a measure of the extensibility of the dumbbell and R is the length of the non-dimensionalized dumbbell end-to-end vector $\boldsymbol{R}$. The full set of equations for the FENE model includes a Fokker-Planck equation for the probability density function of the dumbbells configuration at each point within the flow domain [11]. Introducing the so-called Peterlin approximation, one can obtain a simplified set of partial differential equations for the viscoelastic component defining the FENE-P model. The FENE-P equations exhibit a shear-thinning viscosity and have good stability properties for the numerical calculations. When ($L^2 \to \infty$), one recovers the Hookean model that leads to the classical Oldroyd-B equations. By introducing some further phenomenological modification, Chilcott M. D. and Rallison J. N. [12] obtained the FENE-CR model which predicts a constant shear viscosity. Let us note that the steady extensional properties of FENE-CR and FENE-P models are the same, but do not correspond to the true FENE model, as demonstrated by Keunings [13]. However, this is not true for the transient stress growth of the two models, that is different at large De, with the FENE-CR model showing a small overshoot.

The FENE-CR model is defined by the following set of equations

$$\begin{cases} \mathbf{A} + \lambda(1 - \mathrm{tr}\mathbf{A}/L^2)\overset{\triangledown}{\mathbf{A}} = \mathbf{I}, \\ \\ \mathbf{T}_V = \dfrac{\eta_V}{\lambda}\left[\dfrac{\mathbf{A}}{1 - \mathrm{tr}\mathbf{A}/L^2} - \dfrac{\mathbf{I}}{1 - \mathrm{tr}\mathbf{I}/L^2}\right], \end{cases} \tag{5}$$

where λ is the relaxation time, η_V is the viscoelastic viscosity coefficient and $\mathbf{A}$ is the non-dimensional configuration tensor $< \boldsymbol{RR} >$, the configuration space average of the dyadic product of the vector $\boldsymbol{R}$. The symbol $\triangledown$ in (5.a) stands for the upper-convected derivative. Let us note that the last term of (5.b) is often incorporated into the pressure, but it is introduced here in order to obtain a vanishing $\mathbf{T}_V$ for the fluid at rest.

Our mathematical viscoelastic problem consists of finding the velocities, the pressure and the configuration tensor in the domain Ω such that the conservation and constitutive equations are satisfied under suitable boundary conditions for the velocities and the configuration tensor.

2.2 The Free Surface Viscoelastic Problem

Let us assume that Ω is an unknown deforming domain. In particular, we assume that part of the boundary, $\partial\Omega_{\text{FREE}}$, is a free surface.

If Ω is two-dimensional, the free surface can be characterized by a geometrical degree of freedom h, which is a function of time and of the curvilinear coordinate of the initial free surface. This function h can be viewed as the current displacement of the free surface for a given position and at a given time along the normal of the initial surface. To be more precise, the direction of displacement may be arbitrary as long as the displacement does not become tangent to the free surface. Here, we decide to define h as the normal displacement to the initial surface.

In order to obtain a well posed problem, it is well known that we have to impose both the dynamic and the kinematic conditions along the free surface.

- On one hand, continuity of the contact force along the free surface leads to the dynamic condition

  $$\sigma \cdot \boldsymbol{n} = -(p_{\text{ext}} + \gamma(R_1^{-1} + R_2^{-1})) \cdot \boldsymbol{n}, \tag{6}$$

  where p_{ext} is the exterior pressure, γ is the surface tension coefficient and $\boldsymbol{n}$ is the outward unit vector normal to the boundary $\partial\Omega_{\text{FREE}}$. The surface tension relates the normal force with the principal radii of curvature of the interface, R_1 and R_2. The normal vector and the radii of the curvature can be written as expressions of the function h. By integrating by parts, we obtain the weak formulation of the dynamic condition initially proposed by Ruschak K. J. [14] and extended by Keunings R. [15] for the axisymmetric case.

- On the other hand, the fact that the free surface is a material line, leads to the kinematic condition

  $$\frac{Dh}{Dt} = 0. \tag{7}$$

  This relationship provides the additional equation required to calculate the unknown position h of the free surface.

3 Numerical Simulation of the stretching device

Now, we describe the boundary conditions used to calculate the time dependent flow of a viscoelastic fluid in the filament stretching apparatus proposed by Sridhar et al. [10]. In such a device, an initially cylindrical fluid sample is stretched between two plates. The

shape of the fluid column and the force measured along the lower plate as a function of time can be used for the characterization of the extensional viscosity of the sample. The basic parameters of the device are shown in Fig. 1.

The typical function of interest for the rheometer is the Hencky strain as a function of time. The Hencky strain is defined as follows

$$\epsilon \triangleq \ln\left[\frac{L(t)}{L_0}\right], \tag{8}$$

where $L(t)$ is the length of the filament, and $L_0 = L(0)$. Similarly, R_0 is the initial radius of the filament and $R(t)$ is the minimal radius as a function of the time.

By imposing an exponential rate of separation between the two plates, i.e. by assuming that $L(t) = L_0 \exp(\dot{\epsilon}t)$, one hopes to do experiments under constant stretch rate conditions rather than under constant force. The constant stretch rate is denoted by $\dot{\epsilon}$, and the Hencky strain becomes a linear function of time:

$$\epsilon = \dot{\epsilon}t. \tag{9}$$

In our calculations, we neglect inertia and gravity. With this assumption, the flow is not only axisymmetric but also exhibits symmetry with respect to an horizontal midplane between the plates. In the next section, we will demonstrate that we can neglect gravity and inertia if the extensional viscosity is very high compared to the stresses induced by shear viscosity. Finally, we also demonstrate that the same condition has to be satisfied in order to obtain useful experimental results from the stretching device. Therefore, the computational domain is reduced to the area depicted in Fig. 2.

In order to describe the boundary conditions of the viscoelastic free surface problem, we consider the following subsets of the boundary $\partial\Omega$:

- $\partial\Omega_{\text{PLATE}}$, the upper side of the domain, represents the moving plate where the velocity is prescribed. A no-slip condition is applied and the velocity is imposed as follows

$$\begin{aligned} w &= \frac{\dot{\epsilon}L_0}{2}\exp(\dot{\epsilon}t), \\ u &= 0, \end{aligned} \tag{10}$$

  where L_0 is the initial length of the whole sample.

- $\partial\Omega_{\text{SYM}}$, the portion on which symmetry conditions are applied, i.e. vanishing normal velocity and tangential stress,

- $\partial\Omega_{\text{FREE}}$, the free-surface,

- $\partial\partial\Omega_{\mathrm{UP}}$, the point defined by the intersection of the free-surface and the upper moving plate. The position of this point of the free-surface is prescribed to be attached to the end of the plate. In other words, the free-surface is not allowed to slip along the plate,
- $\partial\partial\Omega_{\mathrm{BOTTOM}}$, the point defined by the intersection of the free-surface and the horizontal midline. At this point, one prescribes that the free-surface is vertical.

Initially, the computational domain is rectangular, and the fluid is assumed to be at rest. That means that $\boldsymbol{v} = \mathbf{0}$ and $\mathbf{T}_V = \mathbf{0}$ for $t < 0$. The second equality involves that for the initial $\mathbf{A}$, we take the tensor unity.

A mixed Finite Element Method (FEM) with the configuration tensor, the velocity, the pressure and the geometrical unknowns as variables, is used. Standard Galerkin weak formulation is derived with the quadrilateral finite element developed by Marchal J. M. and Crochet M. J. [16]: the pressure, the velocity and the configuration tensor are approximated by linear, quadratic and 4×4 sub-linear interpolations respectively. However, we observe that we obtain the same results by using quadratic interpolation for the configuration tensor. Such a choice is efficient in terms of CPU and memory requirements. Mesh refinement analysis has been performed.

For the time integration, we use a predictor-corrector scheme. At each time step, a prediction of the solution is calculated with the Euler explicit scheme. This first estimate is then corrected with the Euler implicit scheme. The implicit equations are solved by Newton's method. The next time step is then selected such that the difference between predicted and corrected solutions is kept under a specified value. More details can be found in [17, 18]. The initial shape of the domain is a rectangle, and the sample is at rest before the beginning of the stretching.

A moving grid algorithm is used to avoid overdistorded elements due to the boundary motion and to maintain a good nodes distribution in the deformed mesh. We solve the Thompson transformation [19] in order to take advantage of the smoothing properties of this elliptic operator. Standard Dirichlet boundary conditions are applied on the coordinates, except along the axis of symmetry where Neumann conditions are introduced for the tangential component. Furthermore, a slight modification of the remeshing rule near the upper plate is introduced in order to maintain a high density of elements where the free-surface shape is more complex. In order to handle surface tension, a quadratic continuous representation is used for both the geometrical unknowns and the coordinates.

4 Numerical Results

In most calculations, inertia and gravity are neglected and the parameters of both viscoelastic and Newtonian calculations are summarized in the following table. We use

material parameters identified on the basis of steady shear data [7].

ρ (density)	890 (kg.m^{-3})
$\dot{\epsilon}$ (stretch rate)	1.6 (s^{-1})
L_0 (initial length)	2 10^{-3} (m)
R_0 (initial radius)	3.5 10^{-3} (m)
γ (surface tension coefficient)	28.9 10^{-3} (N.m^{-1})
Newtonian calculations	
η (shear viscosity)	98 (Pa.s)
FENE-CR calculations	
η (shear viscosity)	105 (Pa.s)
η_N (solvent viscosity)	35.7 (Pa.s)
η_V (polymer viscosity)	69.3 (Pa.s)
λ (relaxation time)	2.0 (s)
L^2 (extensibility dumbbell coefficient)	4325.5

Table 1: Material parameters for a Polyisobuthylene/Polybutene Boger fluid [7].

Now, let us define the dimensionless numbers that can be used for analysing the numerical results. The transient Trouton ratio Tr scales the transient extensional viscosity to the shear viscosity. The Deborah number De characterizes the elastic forces with respect to the viscous terms. The capillary number Ca balances viscous and surface tension forces. The Bond number characterizes the ratio of gravitational forces to capillary forces. Finally, the Reynolds number Re characterizes inertia.

$$Tr = \frac{\overline{\eta}^+}{\eta_0},\ De = \lambda\dot{\epsilon},\ Ca = \frac{\eta\dot{\epsilon}R}{\gamma},\ Bo = \frac{\rho g L R}{\gamma},\ Re = \frac{\dot{\epsilon}L^2\rho}{\eta}.$$

It is obvious that the extensional viscosity is the most appropriate quantity to the study of the present flows. Therefore, we use the ratios Re/Tr, $Ca.Tr$ and $Bo/(Ca.Tr)$ to characterize inertia, surface tension and gravity with respect to extensional stresses.

4.1 Stretching flow of a viscoelastic fluid

The shape of the filament, obtained by numerical simulation with the FENE-CR model, is drawn at different times of the calculation in Fig. 3. For relatively large values of the

time t, we see that the filament nearly has the shape of a cylindrical pillar which enlarges near both plates. The formation of the pillar may be explained by the high extensional viscosity of the fluid:

- As a consequence of the high extensional viscosity, a small increase of the deformation leads to a dramatic increase of the stress. This effect tends to distribute the deformation equally in the filament. Therefore, the fluid sample tends to a cylindrical shape, and one also tends to a perfectly extensional flow.
- On the other hand, the high extensional viscosity of the fluid leads to a sucking effect along the plates: the force in the filament is very important and draws away the fluid adhering to the plates. It follows a very steep transition from the cylindrical portion to the adhesion area, and a very strong deformation of the mesh in that region.

The sucking effect is a source of numerical difficulties. A modification of the remeshing rule has been introduced in order to maintain a high density of elements in the transition area. Nevertheless, such a distorsion leads to dramatic deformations of elements and all viscoelastic calculations failed before the time reached the maximum time of the experimental data. In Fig. 4, we see that some elements close to the upper plate become almost triangular at the end of the calculation. As suggested by referee, we also believe that the sucking effect may also be connected to the instabilities observed by McKinley where the fluid forms fibrils near the end plates.

We also analyse the profile of the extensional component of the tensor $\mathbf{A}$ in figure 5. We plot the ratio A_{zz} as a function of r on the mid-plane section. We see that the stretching is more important along the free surface. This effect probably is related to the non purely extensional flow at the beginning of the stretching.

The almost perfect extensional character of the flow can be observed on the curve of the minimum filament radius as a function of Hencky strain, in Fig. 6. At the end of the numerical simulation, the slope of the curve tends to the theoretical dashed line corresponding to a perfect extensional flow. However, the slopes of the two curves are quite different at the early stages of the stretching. Let us observe that the inflexion of the curve at $\epsilon = 1.6$ probably is the sign of the transition from a more complex flow to an almost perfect extensional flow. In fact, the same observation can be made by analysing the different shapes of Fig. 3.

4.2 Stretching flow of a Newtonian fluid

In Fig. 7, we draw the shape of the filament obtained for a Newtonian fluid at various values of Hencky strain. The contours of the free surface are very different than the ones

obtained with the viscoelastic model. We no longer see any cylindrical portion. The radius varies everywhere along the filament, and has a minimum on the symmetry plane. Similarly, the numerical difficulties due to the suction effect do not appear in this case.

In Fig. 8, we give the minimum filament radius as a function of time. The curve of the minimum radius decreases really faster than the line we could obtain for a purely extensional flow. It follows that the Newtonian flow is very different from the uniformly extensional stretching it previously was assumed to be. Therefore Spiegelberg and al. [9] introduced a simplified lubrication analysis to study the stretching of a Newtonian fluid. They provide an estimate of the effective extension rate, $\dot{\epsilon}' \approx 3\dot{\epsilon}/2$ from the imposed value $\dot{\epsilon}$. On Fig. 8, we found an excellent agreement between the estimate from the lubrication theory and our large scale calculations at the beginning of the stretching. Due to the assumptions of the simplified model, it is quite normal that we observe discrepancies at higher values of the stretching.

4.3 Inertia, capillarity and gravity can often be neglected

In this section, we show that we can neglect inertia and gravity in most calculations. It is clear that if inertia and gravity are taken into account, the filament is not divided by a horizontal symmetry plane. Therefore, the axisymmetric calculation has to be performed on the whole filament, which implies an increase of CPU and memory requirements by a factor two. We consider both the viscoelastic and Newtonian cases studied in the previous sections.

- Using a viscoelastic model, we first perform the calculation neglecting inertia and gravity. Then, we calculate the same problem, taking into account inertia and gravity. In Fig. 9, we give the force measured on the lower plate as a function of time for both cases. A detailed analysis of the results shows that the shift between the two curves is approximately equal to the weight of the sample divided by two, and is small compared to the value of the force.

- Let us now perform the same numerical experiments with a Newtonian model. Results are given in Fig. 10. The shift between the two curves is again approximately equal to the sample weight divided by two. We observe that the force measured on the lower plate for the calculation without inertia and gravity decreases very quickly and that the extensional force becomes much smaller than the value of the sample weight at the end of the stretching. Now, if we take inertia and gravity into account, this fact leads to a negative total force for large values of the time.

Inertia and gravity may be neglected in the first calculation with a viscoelastic model, but not in the second with a Newtonian one. This observation is related to the fact that the extensional viscosity of the viscoelastic fluid is very important compared to its

shear viscosity, which results in high Trouton ratios, while the extensional and shear viscosities of a Newtonian fluid are related by a constant Trouton ratio. Inertia terms are neglectible in our calculations: the maximum value of Re/Tr is approximately 0.2 at the end of the Newtonian stretching. The effect of gravity is very small in viscoelastic calculations ($Bo/(Ca.Tr) \approx 10^{-2}$) and may be important for the Newtonian calculations ($Bo/(Ca.Tr) \approx 4$ at the end of the calculation).

A similar conclusion can be drawn for the capillary forces: the dimensionless group $Ca.Tr$ ranges from 20 to 400 for the viscoelastic calculation, while at the end of the stretching of the Newtonian fluid, $Ca.Tr$ is approximately 1.

We conclude that only with strain hardening, the minimum radius of the filament decreases approximately as for a uniaxial extensional flow. Then, it is difficult to find a good interpretation of the force measured along the lower plate in other cases. Therefore, inertia, capillarity and gravity may be neglected for all cases where the extensional rheometer is able to produce useful results (i.e. extensional viscosity is high).

4.4 Improved estimate of the extensional viscosity

The main quantity of interest from the experimental data provided by the filament stretch rheometer is the extensional viscosity. In order to estimate this quantity, one measures F, the normal force applied to the lower plate. Assuming that the flow is close to uniaxial extension at the median plane, the extensional tension inside the filament is then estimated by

$$\tau \simeq \frac{F}{\pi R^2}\,, \tag{11}$$

where R is the radius of the filament. Finally, approximating the extensional rate by the stretch rate $\dot{\epsilon}$, one is able to calculate an extensional viscosity by

$$\overline{\eta}^{+}+ \simeq \frac{\tau}{\dot{\epsilon}}. \tag{12}$$

In fact, the flow is not purely extensional (in particular, at the beginning of the stretch). Only the middle of the domain is in extension, and the local extension rate in the middle of the sample is greater than the Hencky strain rate. A central question is of course to determine what such an estimate means. The problem can be addressed by the numerical simulation of the whole experiment. It can also be addressed by a better estimate of the extensional rate along the center line. For example, we consider only a small material cylindrical part of the filament. If we define l as the length of this cylinder, the volume conservation law leads to the following relationship:

$$lR^2 = l_0 R_0^2.$$

Therefore, one is able to derive a better approximation for both the extension strain and the extension rate:

$$\epsilon' \simeq \ln \frac{l}{l_0} = \ln \frac{R_0^2}{R^2},$$

$$\dot{\epsilon}' \simeq -2\frac{\dot{R}}{R}. \tag{13}$$

A second estimate of the extensional viscosity can be written as

$$\overline{\eta}^+ \simeq \frac{\tau}{\dot{\epsilon}'}. \tag{14}$$

The definition of this estimate can be clearly correlated with the work of Solomon and Muller [6] who demonstrate the difference between radial and axial measures of strain rate.

Finally, a third estimate of the extensional viscosity is provided by the lubrication model of Spiegelberg and al. [9]

$$\overline{\eta}^+ \approx 3 + \frac{R_0^2}{L_0^2} \mathrm{e}^{\frac{-7\epsilon}{3}}. \tag{15}$$

In Fig. 11 the extensional viscosities of a Newtonian fluid as a function of the Hencky strain is drawn from calculations in which gravity and inertia terms have been neglected, using (12) and (14). We also draw the curve of the lubrication model using (15). One can observe that the slopes of all estimates of extensional viscosity are approximatively similar. However, the first approximation is distant from the horizontal line corresponding to the Trouton ratio. Therefore, the second estimate of the extensional strain rate appears to be more realistic. We also observe that the lubrication theory agrees with our improved estimate of the Trouton ratio at the beginning of the stretching. The comparison of our two estimates of the Trouton ratio has also been done for the viscoelastic fluid in Fig. 12. It demonstrates that both approximations of the extensional viscosities are similar for large times. Some people have proposed an approach to avoid the nonuniformities of Hencky strain rate during the stretching [6, 9] by selecting a modified evolution for the velocity of the upper plate.

4.5 Comparison with experimental results

In Fig. 13, we compare the forces as a function of time for a viscoelastic fluid, obtained respectively by the numerical calculations and by the measurements of McKinley. The large discrepancy at the initial times is due to the delay (100 ms) of the measurement device. The high value of the force at the beginning of the stretching is also explained by the poorly extensional character of the sample deformation.

Now, let us compare in Fig. 14 both the minimum filament radius as a function of time obtained by the numerical calculations and by image analysis of the experiments. One obtains a very good qualitative agreement and in particular, the numerical simulation reproduces the slope change observed in experimental data.

In Fig. 15, we investigate the influence of the material parameters of the constitutive equation for different kind of samples. In particular, we also perform the same calculation for the fluid defined in the following table.

η (shear viscosity)	98 (Pa.s)
η_N (solvent viscosity)	32.67 (Pa.s)
η_V (polymer viscosity)	65.33 (Pa.s)
λ (relaxation time)	2.9 (s)
L^2 (extensibility dumbbell coefficient)	4325.5

Table 2: Material parameters for a Polyisobuthylene/Polybutene [7] Boger fluid.

For $\epsilon > 1$, the curves obtained with the numerical calculation are similar to the experimental data given by McKinley.

In figure 16, we also investigate the effect of the initial gap between the plates. The major difference between the curves occurs in the area $\epsilon < 1$, and consists mainly of a shift of the initial value. This fact is due to the more non-extensional character of the deformation at the beginning of the stretching when the gap is small. Qualitatively, the influence of a modification of the initial gap is in good agreement with experimental results.

5 Conclusions

We show that the rheometer of Sridhar performs well with fluids exhibiting a high extensional viscosity. For low extensional viscosity fluids, the obtained flow is very far from extensional, and it is difficult to give a straightforward interpretation of the results.

We limit ourselves to the set of parameters provided by the shear data. In particular, we do not attempt to modify the parameters in order to match both shear and extensional experimental data. However, we think that a suitable set of parameters would certainly lead to a better agreement between numerical and experimental results. We could also further investigate the effect of surface tension, gravity and inertia.

Acknowledgments

This paper presents research results of the Belgian Programme of Interuniversity Attraction Poles initiated by the Belgian state, Prime Minister's Office for Science, Technology and Culture. We are grateful to McKinley G. H. for providing experimental data prior to publication. The scientific responsability rests with its authors.

References

[1] Debbaut B. and Crochet M. J. Extensional effects in complex flows. *Journal of Non-Newtonian Fluid Mechanics*, 30:169–184, 1988.

[2] Purnode B. and Crochet M. J. Flows of polymer solution through contractions, part II: Flows of fluid M1 through axisymmetric contractions. *to be published in Journal of Non-Newtonian Fluid Mechanics.*

[3] Shipman R. W. G., Denn M. M., and Keunings R. Mechanics of the "falling plate extensional" rheometer. *Journal of Non-Newtonian Fluid Mechanics*, 40:281–288, 1991.

[4] Purnode B. and Crochet M. J. Polymer solution characterization with the FENE-P model. *to be published in Journal of Non-Newtonian Fluid Mechanics.*

[5] Petera J. and Nassehi V. Use of the finite element modelling for the improvement of viscometry results obtained by cone-and-plate rheometers. *Journal of Non-Newtonian Fluid Mechanics*, 58:1–24, 1995.

[6] Solomon M. J. and Muller S. J. The transient extensional behavior of polystyrene-based Boger fluids of varying solvent quality and molecular weight. *Journal of Rheology*, 40:837–856, 1996.

[7] McKinley G. H. Steady and transient motion of a sphere sedimenting through shear-thinning and constant-viscosity elastic fluids. *BSR Annual Award Lecture, IXth International Workshop on Numerical Methods in Non-Newtonian Flows*, 1995.

[8] Caswell B. Report on the IXth International Workshop on Numerical Methods in Non-Newtonian Flows. *Journal of Non-Newtonian Fluid Mechanics*, 62:99–110, 1996.

[9] Spiegelberg S. H., Ables D. C., and McKinley G. H. The role of end effects on measurements of extensional viscosity in filament stretching rheometers. *Journal of Non-Newtonian Fluid Mechanics*, 64:229–267, 1996.

[10] Tirtaatmadja V. and Sridhar T. A filament stretching device for measurement of extensional viscosity. *Journal of Rheology*, 37:1081–1102, 1993.

[11] Bird R. B., Curtiss C. F., Armstrong R. C., and Hassager O. *Dynamic of polymeric liquids*, volume 2: kinetic theory. Wiley, 1987.

[12] Chilcott M. D. and Rallison J. N. Creeping flow of dilute polymer solutions past cylinders and spheres. *Journal of Non-Newtonian Fluid Mechanics*, 29:381–432, 1988.

[13] Keunings R. On the Peterlin approximation for finitely extensible dumbbels. *to be published in Journal of Non-Newtonian Fluid Mechanics.*

[14] Ruschak K. J. A method for incorporating free boundaries with surface tension in finite element fluid flow simulators. *International Journal for Numerical Methods in Engineering*, 15:639–648, 1980.

[15] Keunings R. An algorithm for the simulation of transient viscoelastic flows with free surfaces. *Journal of Computational Physics*, 62:199–220, 1986.

[16] Marchal J. M. and Crochet M. J. A new mixed finite element for calculating viscoelastic flow. *Journal of Non-Newtonian Fluid Mechanics*, 26:77–114, 1987.

[17] Bodart C. and Crochet M. J. The time-dependent flow of a viscoelastic fluid around a sphere. *Journal of Non-Newtonian Fluid Mechanics*, 54:303–329, 1994.

[18] Gresho P. M., Chang S. T., Lee R. L., and Upson C. D. A modified finite element method for solving time-dependent uncompressible Navier-Stokes equations. *International Journal for Numerical Methods in Fluids*, 4:557–598, 1984.

[19] Thompson J. F., Warsi Z. U. A., and Mastion C. W. *Numerical grid generation, foundations and applications.* North-Holland, 1985.

Figures

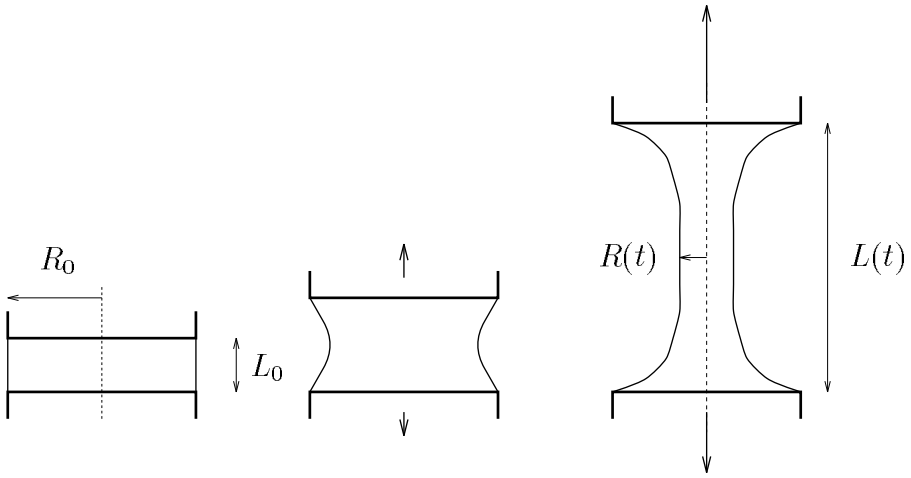

Fig. 1. Schematic of the filament stretching rheometer.

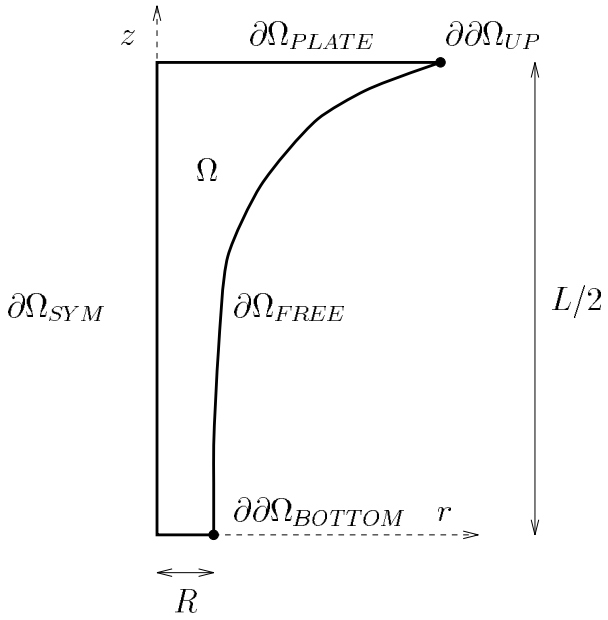

Fig. 2. Geometry for the numerical simulation of the filament stretching rheometer.

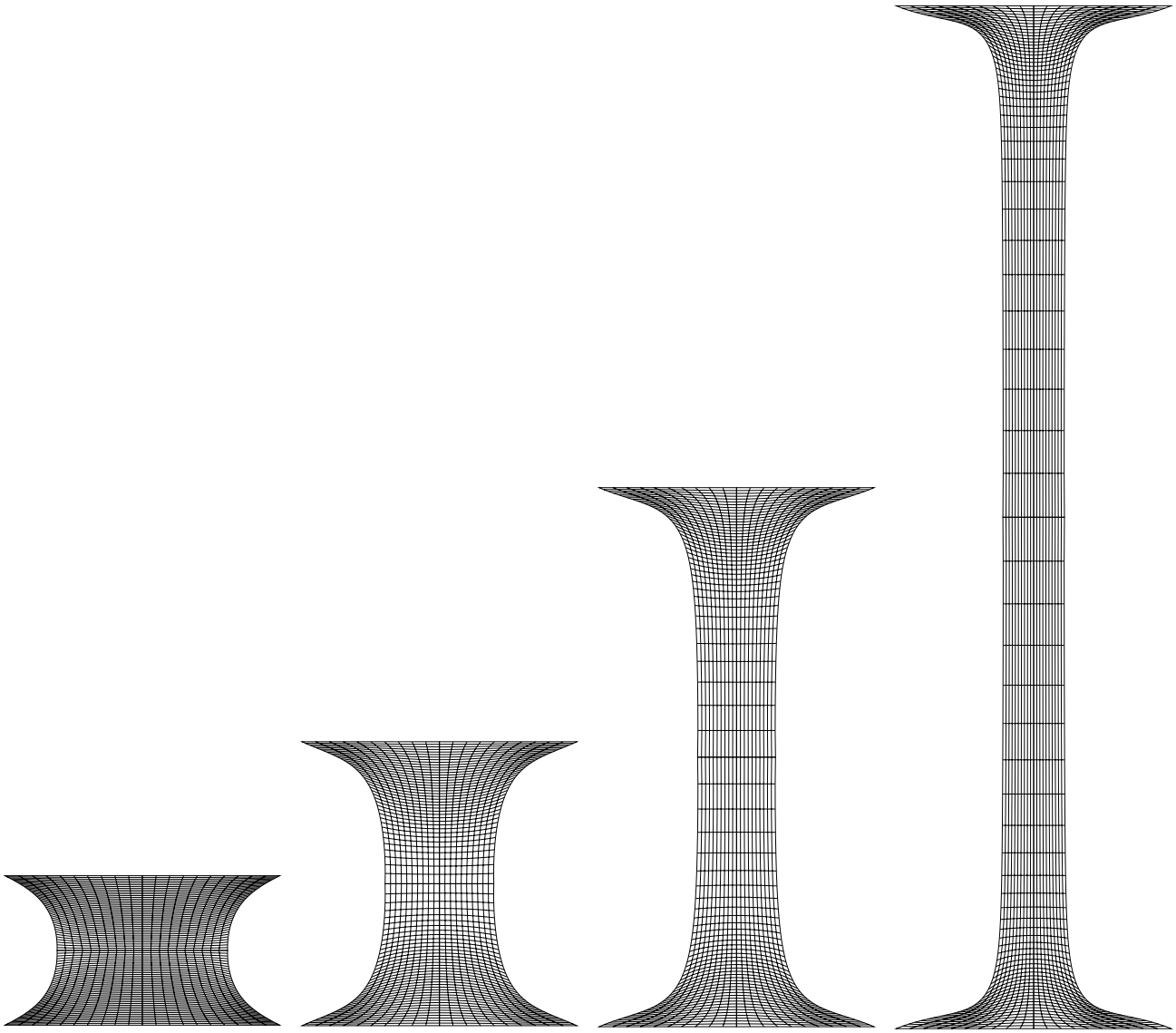

Fig. 3. Viscoelastic calculation: deformation of the sample as a function of the Hencky strain.

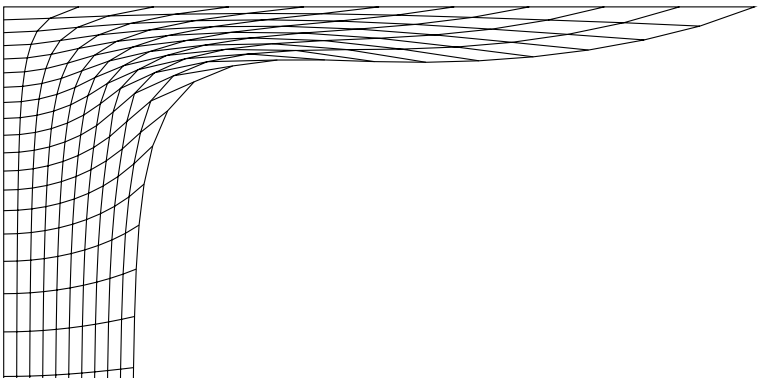

Fig. 4. Viscoelastic calculation: closeup view of the mesh at time $\epsilon = 3.52$. The remeshing rule minimizes the distorsion of the elements, when the suction effect takes place near the plate.

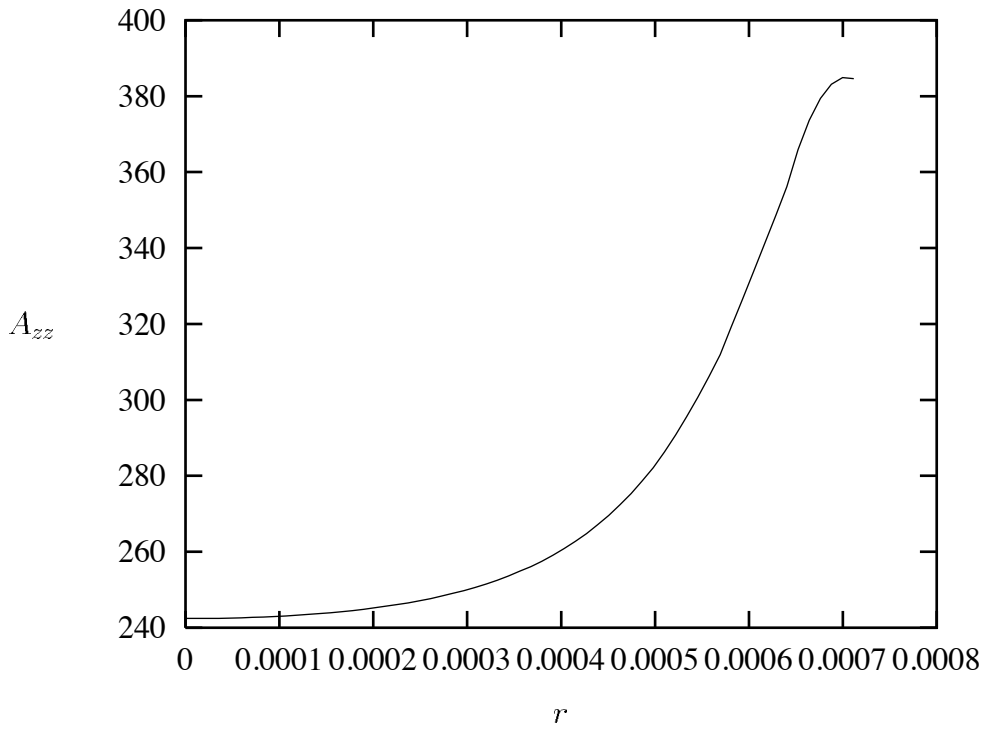

Fig. 5. Evolution of A_{zz} as a function of the radius along the symmetry plane for $\epsilon = 2.88$.

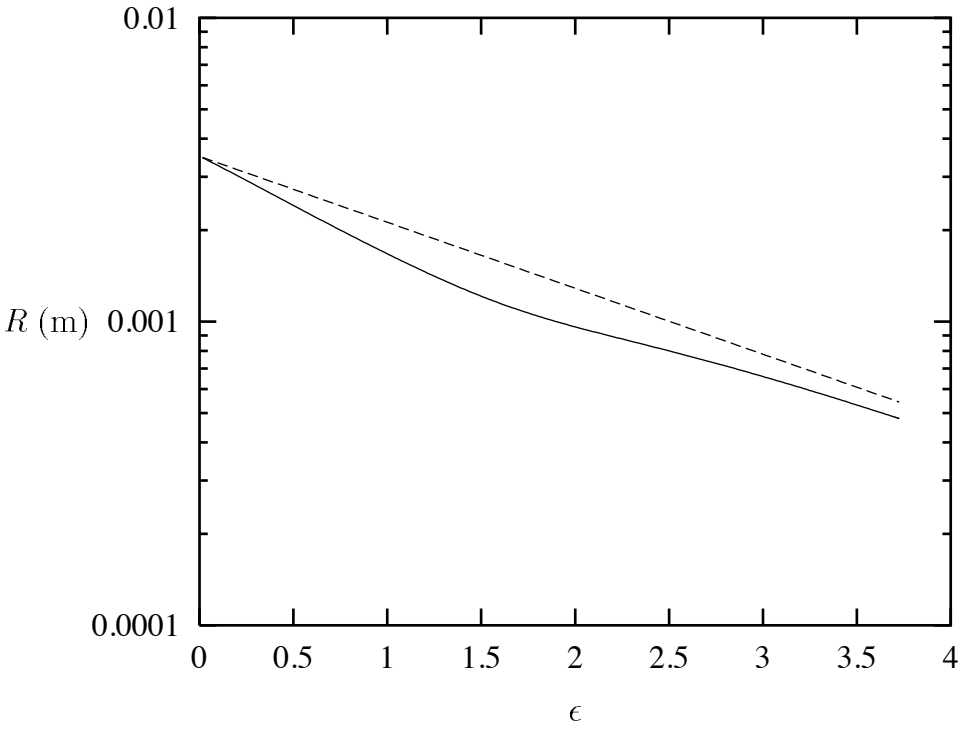

Fig. 6. Viscoelastic calculation: minimum filament radius as a function of the Hencky strain. The dashed line represents the theoretical evolution of the radius for a perfectly uniaxial extension. It is a fair approximation of the real behaviour for large values of the Hencky strain.

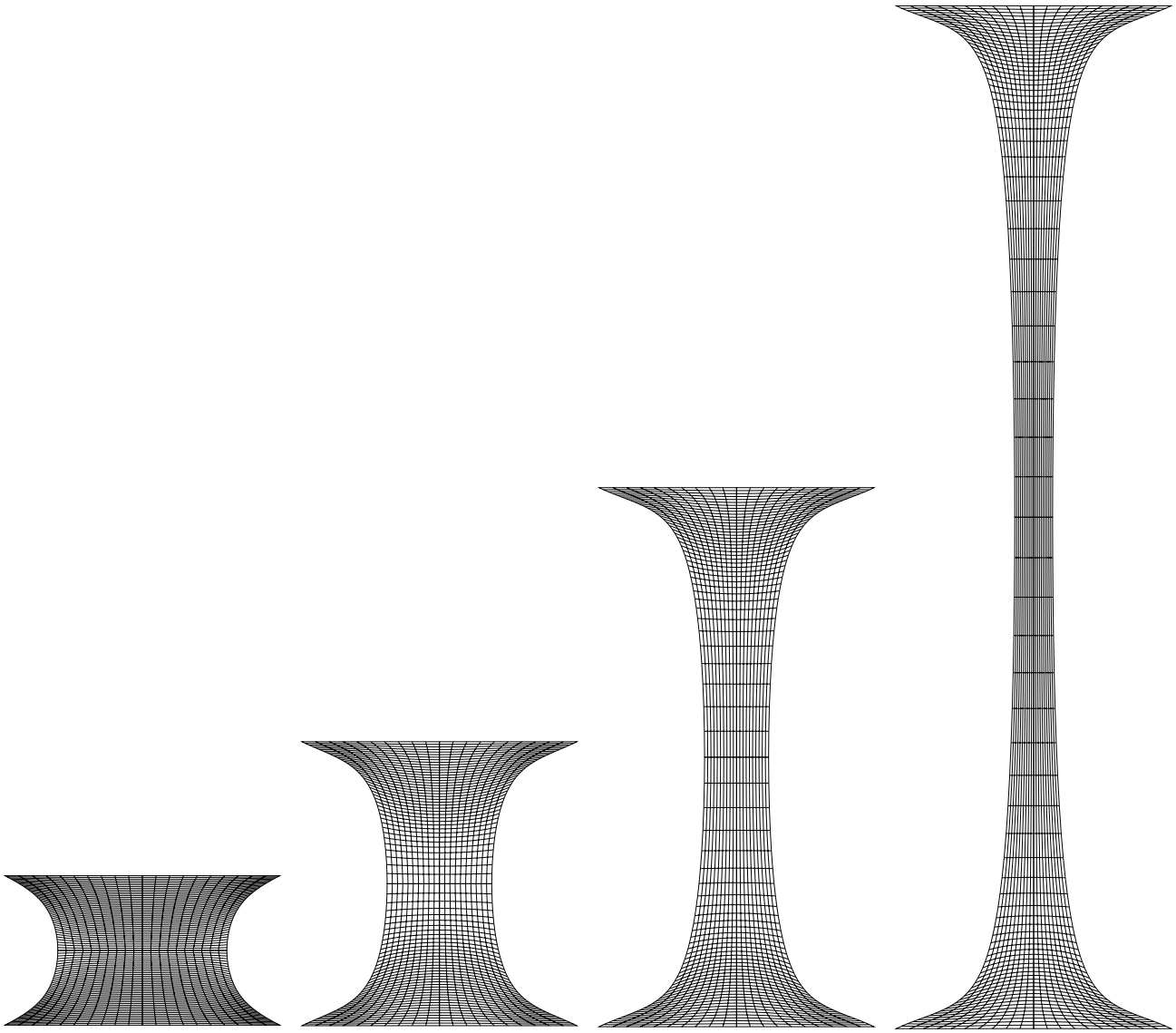

Fig. 7. Newtonian calculation: deformation of the sample as a function of the Hencky strain.

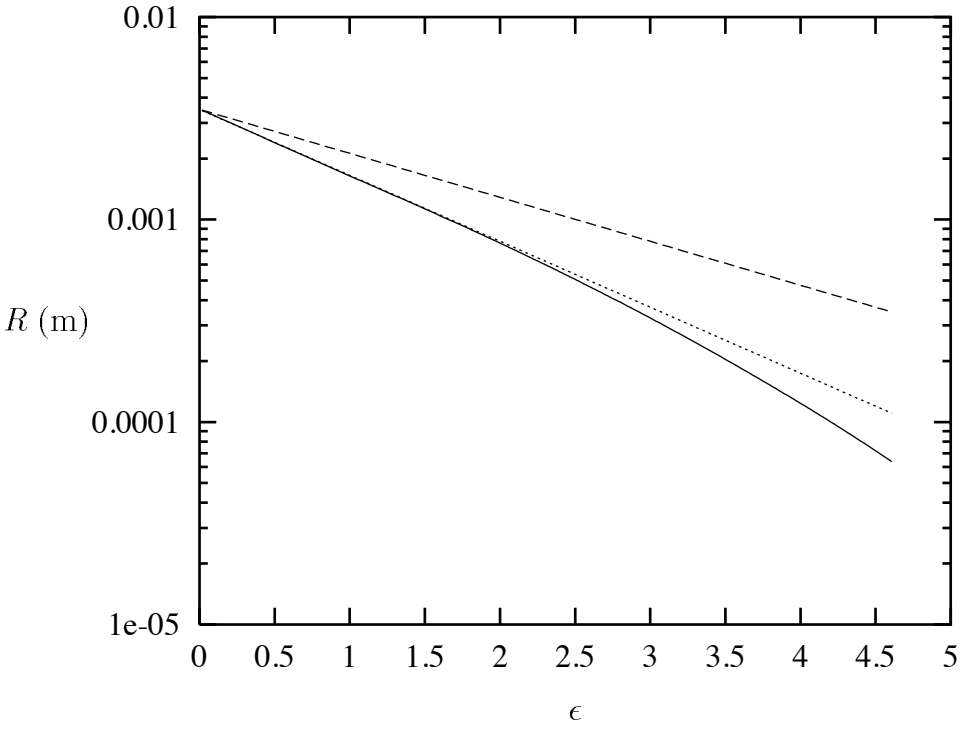

Fig. 8. Newtonian calculation: minimum filament radius as a function of the Hencky strain. The dashed line represents the theoretical evolution of the radius for a perfectly uniaxial extension while the dotted line gives the results predicted with the lubricated model.

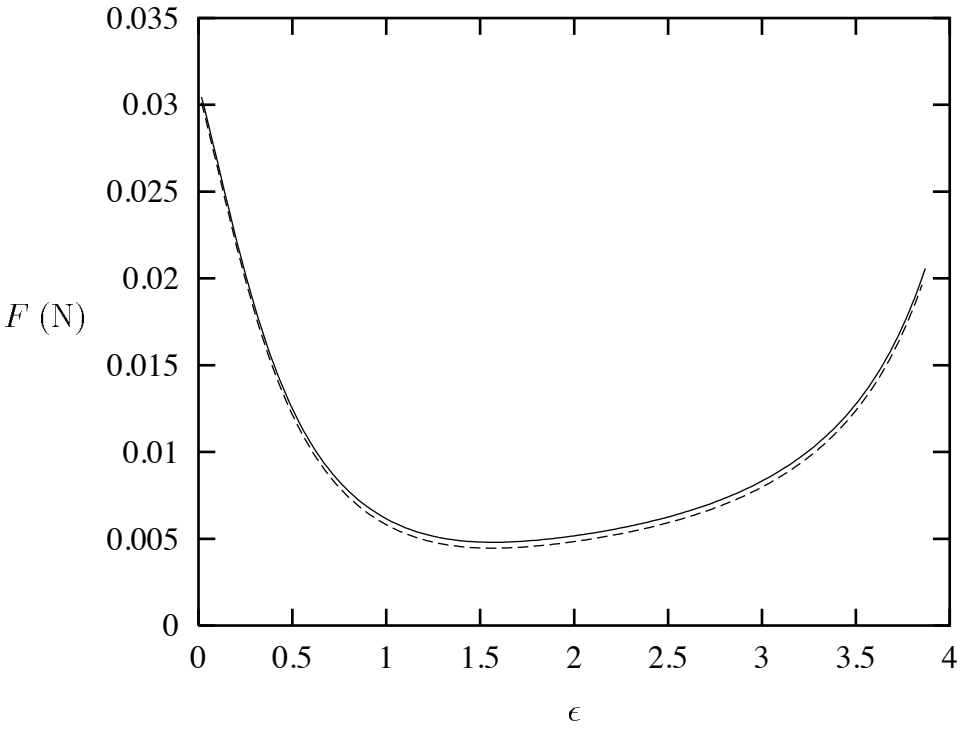

Fig. 9. Viscoelastic calculations: force measured on the lower plate as a function of the Hencky strain. The dashed and the continuous lines give the results when inertia and gravity are taken into account or neglected repectively.

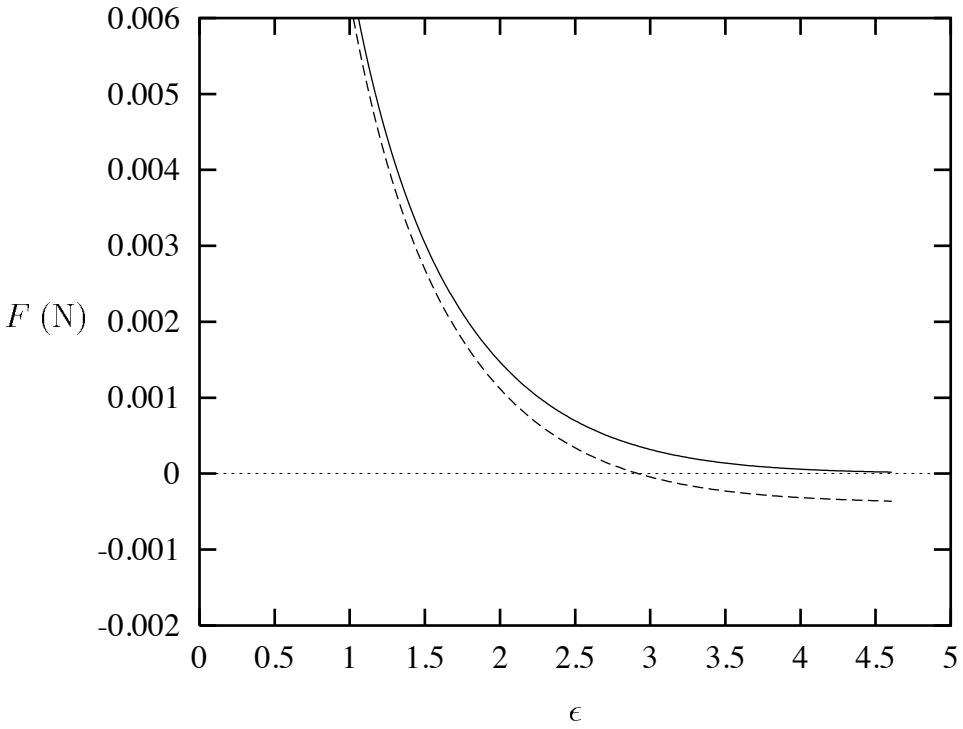

Fig. 10. Newtonian calculation: force measured on the lower plate as a function of the Hencky strain. The dashed and the continuous lines give the results when inertia and gravity are taken into account or neglected repectively.

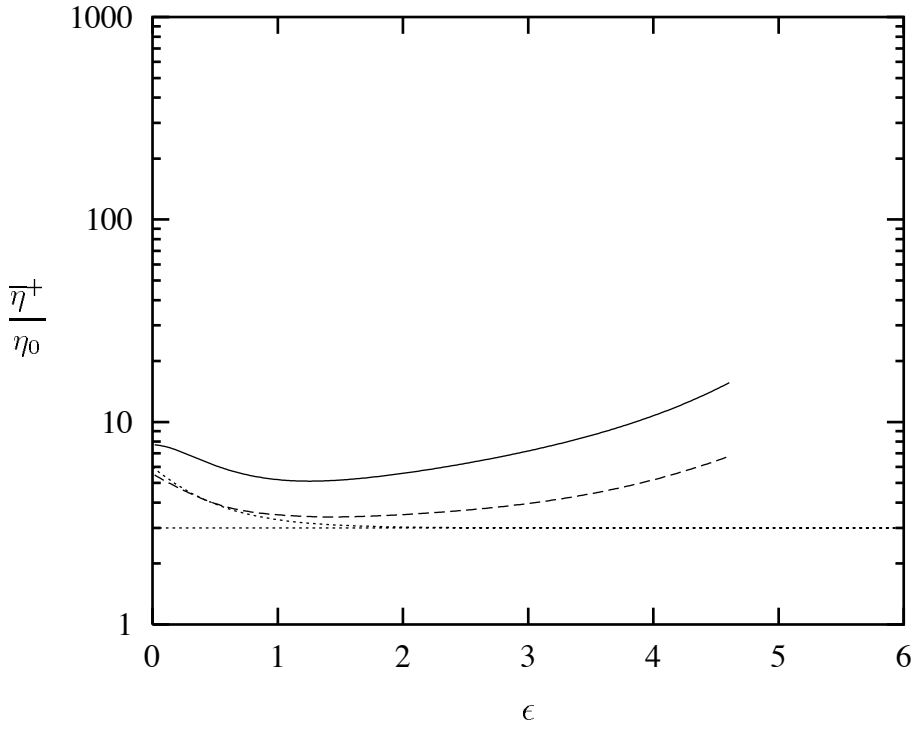

Fig. 11. Newtonian calculation: estimated extensional viscosities as a function of the Hencky strain. The continuous and the dashed lines give the results when the extensional rate is approximated by the stretch rate of the Hencky strain or by a local mid-plane estimation from the radius behaviour respectively. The two dotted lines give respectively the theoretical Trouton ratio ($Tr = 3$) and the results given by the lubricated model.

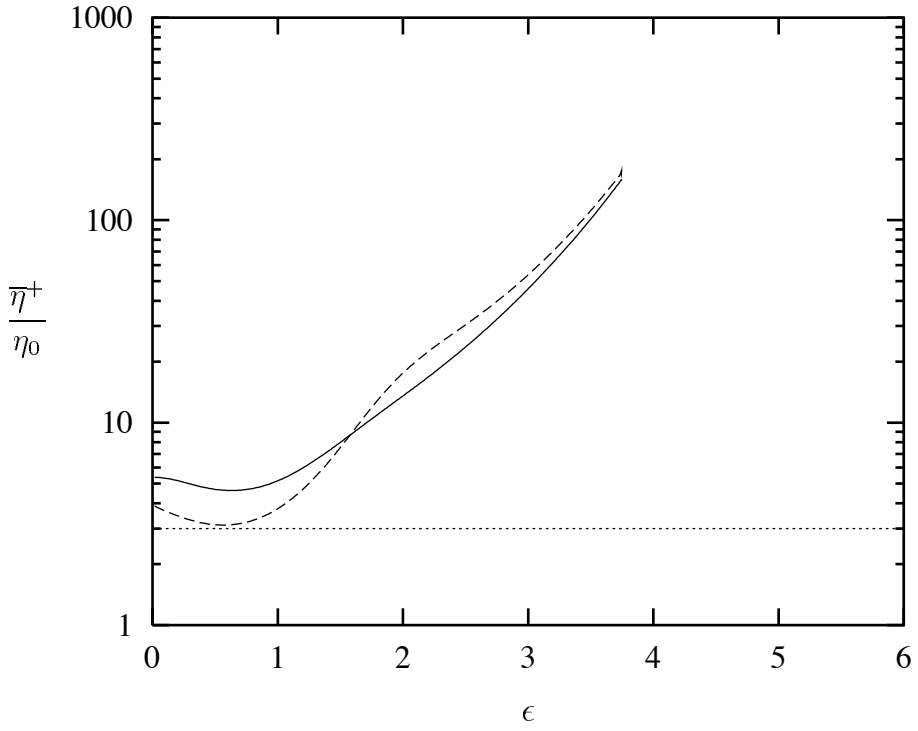

Fig. 12. Viscoelastic calculation: estimated extensional viscosities as a function of the Hencky strain. The continuous and the dashed lines give the results when the extensional rate is approximated by the stretch rate of the Hencky strain or by a local mid-plane estimation from the radius behaviour respectively. Both curves are almost similar, excepted for initial values of the Hencky strain.

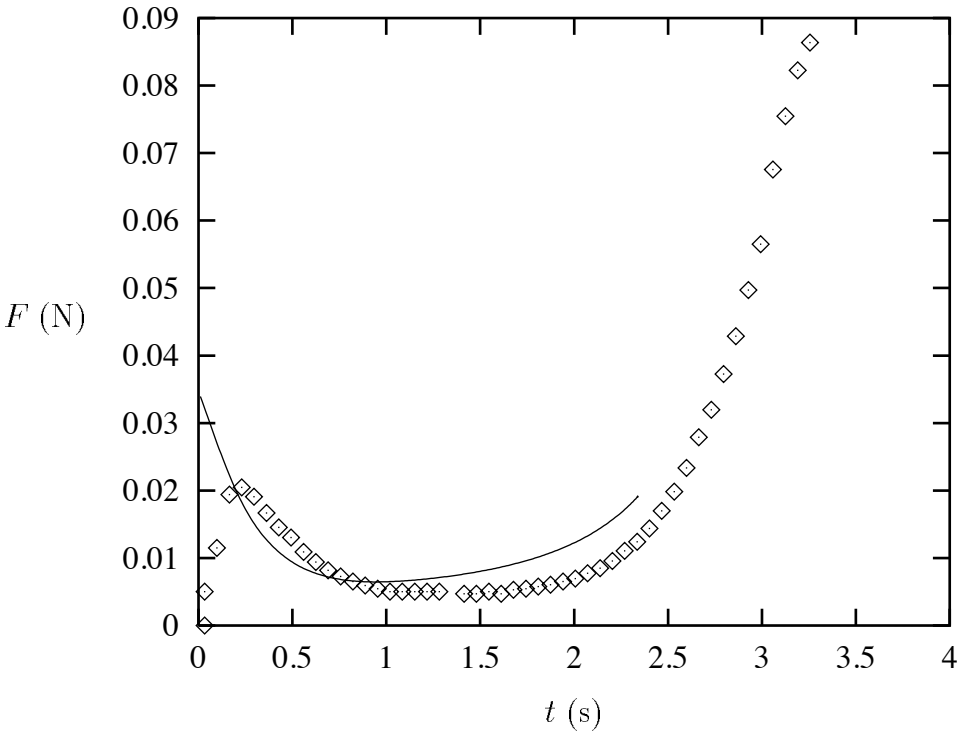

Fig. 13. Comparison with experimental results: force to be exerced on the plate as a function of time. The lines and the symbols give the numerical results and the experimental data respectively.

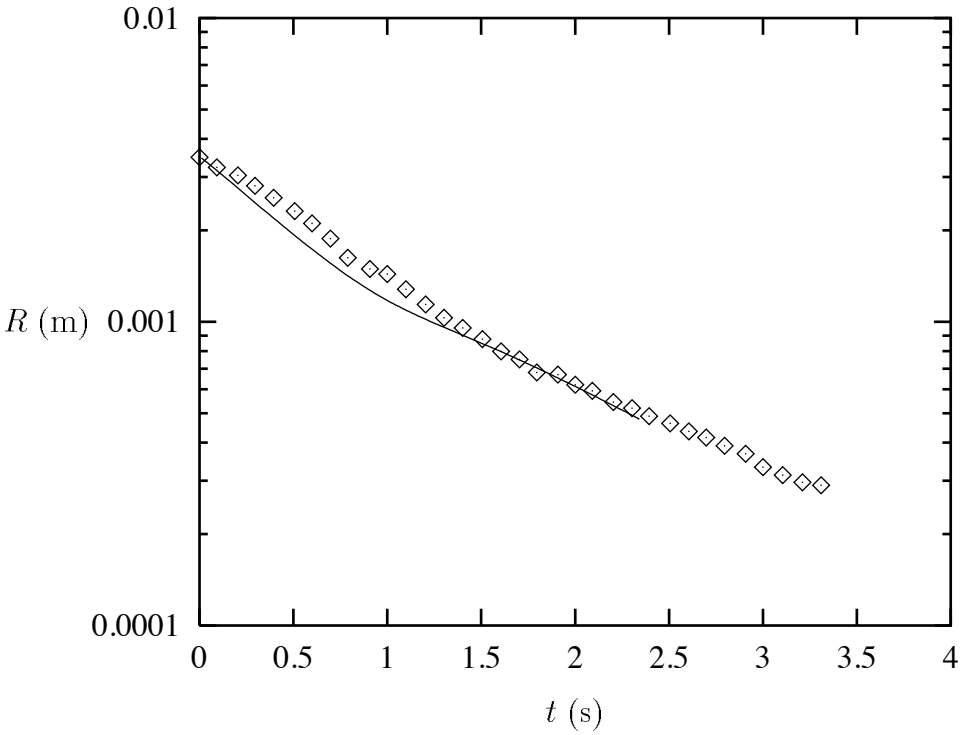

Fig. 14. Comparison with experimental results: minimum filament's radius as a function of time. The lines and the symbols give the numerical results and the experimental data respectively.

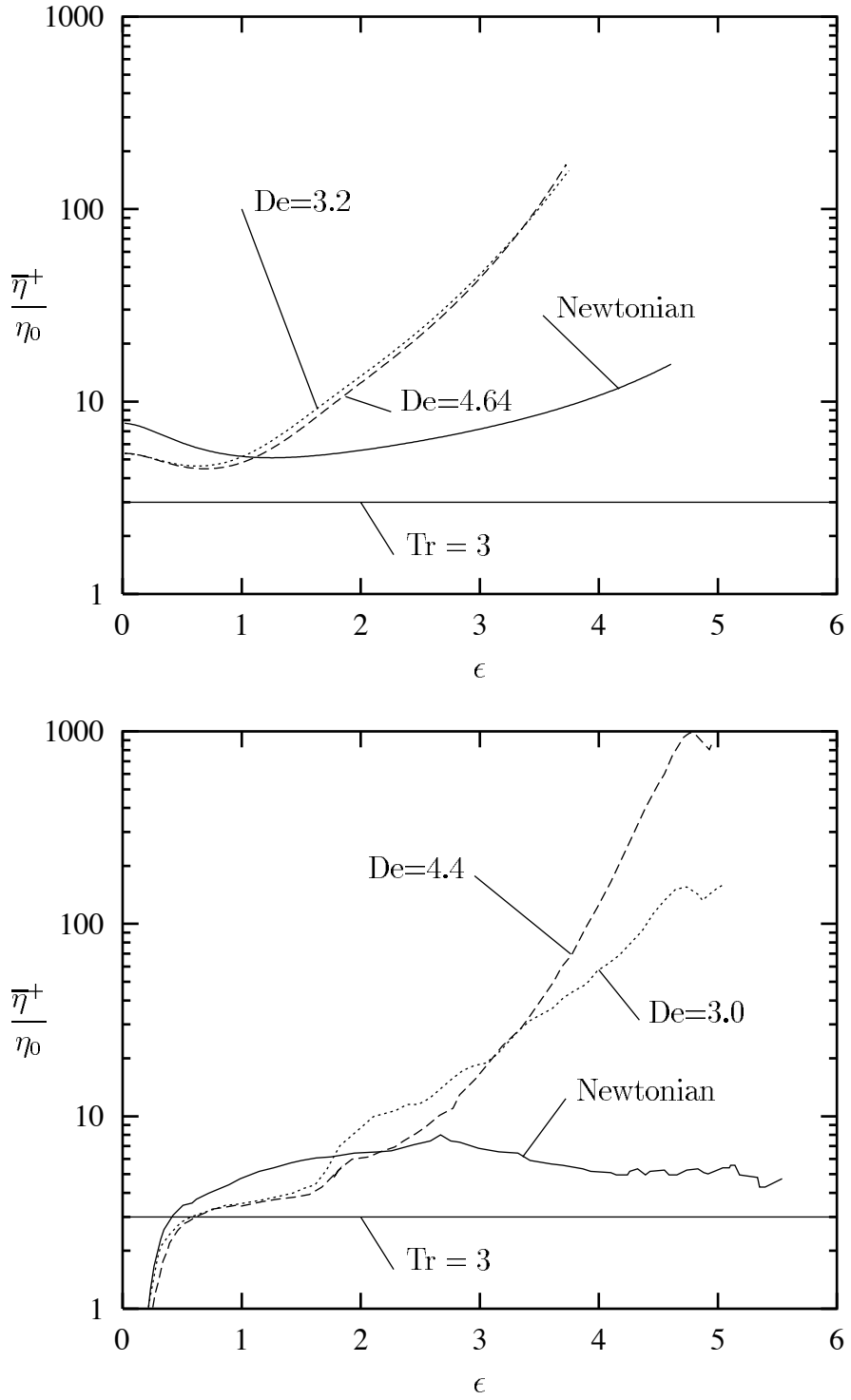

Fig. 15. Comparison with experimental results for different fluids: estimated extensional viscosities as a function of the Hencky strain. The upper and lower parts give the numerical results and the experimental data respectively.

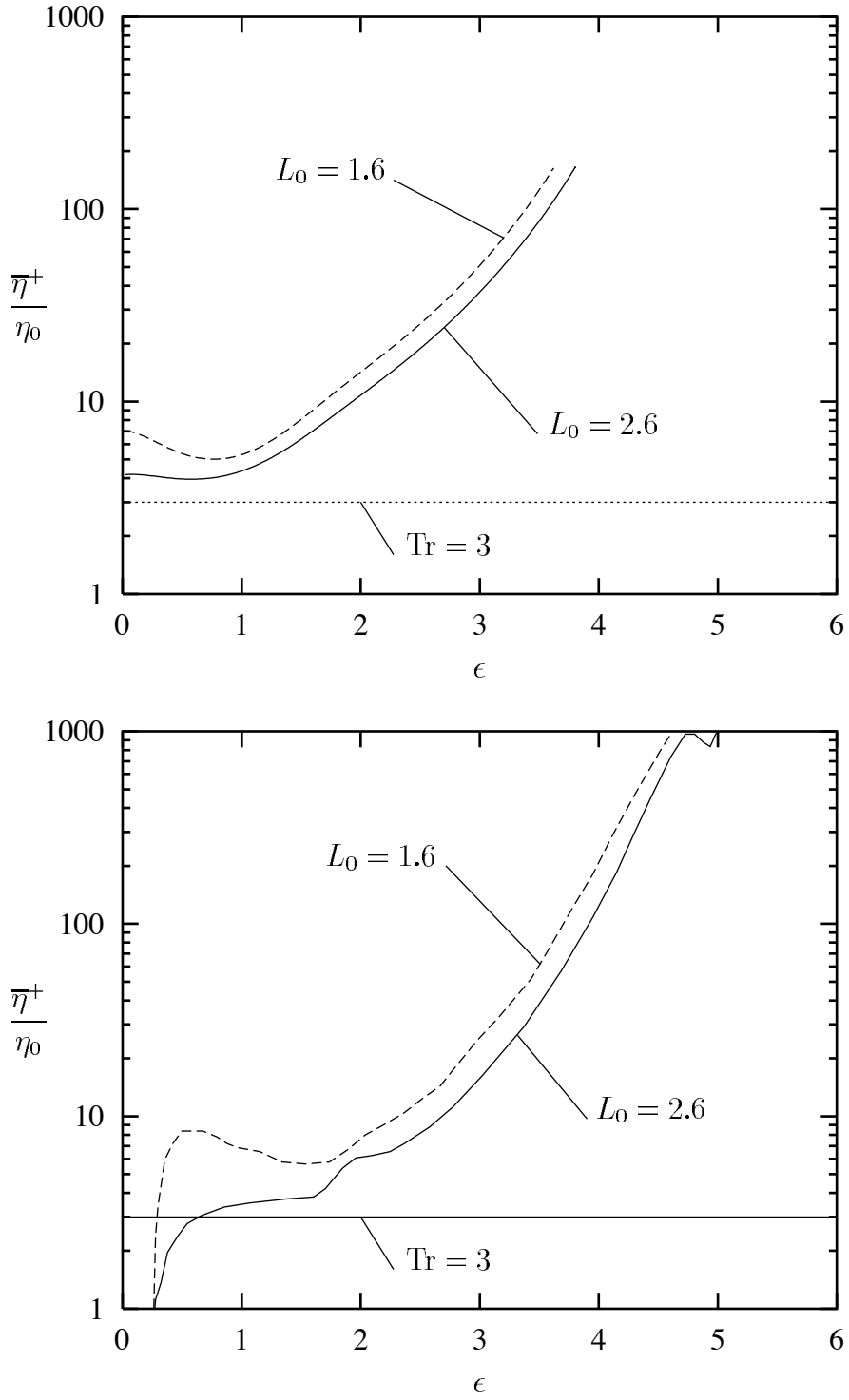

Fig. 16. Comparison with experimental results for different initial lengths: estimated extensional viscosities as a function of the Hencky strain. The upper and lower parts give the numerical results and the experimental data respectively.